

Visualization of Light Elements using 4D STEM: The Layered-to-Rock Salt Phase Transition in LiNiO₂ Cathode Material

Shamail Ahmed, Matteo Bianchini, Anuj Pokle, Manveer Singh Munde, Pascal Hartmann, Torsten Brezesinski, Andreas Beyer, Jürgen Janek,* and Kerstin Volz*

The layered oxide LiNiO₂ (LNO) has been extensively investigated as a cathode active material for lithium-ion batteries. Despite LNO's high gravimetric capacity, instability issues hinder its commercialization. It suffers from capacity loss during electrochemical cycling and is difficult to synthesize without defects. This is related to poor structural stability, leading to decomposition into the parent rock-salt-type oxide. In order to understand such phase transformations and to develop measures to inhibit them, the development of techniques able to image all atoms is crucial. In this study, the use of a fast, pixelated detector and 4D imaging in scanning transmission electron microscopy are explored to tackle this challenge. Selecting specific angular regions in the diffraction patterns and calculating virtual annular bright-field images significantly enhances the contrast of the lithium atoms, such that all atoms are visible even in realistic samples. The developed technique is applied to image the layered-to-rock salt phase transition region. The data show that in this region, nickel atoms are in tetrahedral positions and the oxygen atoms are asymmetrically distributed. Taken together, the results shed light on the phase transformation mechanism at the atomic scale and can guide future research toward stabilizing LNO.

explored because of their higher practical specific capacities compared to conventional LiCoO₂ (LCO).^[6,7] LiNiO₂ (LNO) has the potential to surpass both NCM and NCA in terms of capacity^[8,9] and to be more cost-effective than LCO.^[10] Unfortunately, LNO suffers from rapid capacity fade during electrochemical cycling.^[11] Several causes have been identified, yet the main reason for this degradation lies in the irreversible transformation of the crystal structure into a rock salt-like one, especially at the particles' surface, at low lithium content.^[12,13] So far, the common understanding is that O_{2(g)} and Li₂O are lost from the material, with subsequent Ni reduction and formation of a rock salt-like phase of Li_yNi_{1-y}O. Nevertheless, detailed mechanistic understanding of such phase transformation is missing due to the lack of an atomically-resolved technique able to image all elements in the different phases with high contrast. It is mostly believed that "spinel-like" or "disordered spinel"


1. Introduction

Because of the ever-increasing demand for more efficient energy storage, there is considerable interest in improving current lithium-ion battery (LIB) technology.^[1,2] Ni-rich layered NCM (LiNi_{1-x-y}Co_xMn_yO₂)^[3] and NCA (LiNi_{1-x-y}Co_xAl_yO₂)^[4] cathode active materials (CAMs)^[5] with $x + y < 0.3$ have been widely

regions may be present in between the layered and rock salt ones; however, strong experimental evidence is scarce.^[14] With an improved atomistic understanding of the phase transformation, it could be possible to find ways to circumvent it.

(Scanning) transmission electron microscopy [(S)TEM] has been used extensively to characterize LIB compounds at the atomic scale.^[15–21] High angle annular dark-field (HAADF)

S. Ahmed, Dr. A. Pokle, Dr. M. S. Munde, Dr. A. Beyer, Prof. K. Volz
Materials Science Center (WZMW) and Department of Physics
Philipps-Universität Marburg
Hans Meerwein Strasse
Marburg 35032, Germany
E-mail: kerstin.volz@physik.uni-marburg.de

 The ORCID identification number(s) for the author(s) of this article can be found under <https://doi.org/10.1002/aenm.202001026>.

© 2020 The Authors. Published by WILEY-VCH Verlag GmbH & Co. KGaA, Weinheim. This is an open access article under the terms of the Creative Commons Attribution-NonCommercial License, which permits use, distribution and reproduction in any medium, provided the original work is properly cited and is not used for commercial purposes.

Dr. M. Bianchini, Dr. P. Hartmann, Dr. T. Brezesinski, Prof. J. Janek
Battery and Electrochemistry Laboratory
Institute of Nanotechnology
Karlsruhe Institute of Technology (KIT)
Hermann-von-Helmholtz-Platz 1, Eggenstein-Leopoldshafen 76344
Germany
E-mail: Juergen.Janek@phys.Chemie.uni-giessen.de

Dr. M. Bianchini, Dr. P. Hartmann
BASF SE
Carl-Bosch-Strasse 38, Ludwigshafen 67056, Germany
Prof. J. Janek
Institute of Physical Chemistry & Center for Materials Research
Justus-Liebig-University
Heinrich-Buff-Ring 17, Giessen 35392, Germany

DOI: 10.1002/aenm.202001026

imaging is well known as a TEM technique for high-resolution imaging.^[22] However, the HAADF detector regime is primarily sensitive for the study of heavy elements, since the scattered intensity is directly proportional to the atomic number ($\approx Z^{1.7}$).^[22–24] Light atoms are only weakly or not at all visible in HAADF images, making it difficult to pinpoint their position and quantify them. This gets even more challenging when the light elements are positioned very close to heavier elements.^[25] Contrarily to HAADF imaging, the contrast in annular bright-field (ABF) imaging has a weak $Z^{1/3}$ dependence, making this technique suitable for imaging light elements.^[26]

For CAMs, the difficulties in imaging light elements like lithium and oxygen present major obstacles in understanding structural changes in both pristine and electrochemically cycled samples.^[27,28] Shao-Horn et al.^[29] reported the direct observation of lithium in LCO by recording a focal series using conventional TEM. Unfortunately, strict sample thickness requirements and complex simulation steps make this technique cumbersome. More recently, Lozano et al.^[25] combined aberration-corrected STEM with a pixelated detector to image lithium in $\text{Li}_{1.2}\text{Mn}_{0.6}\text{Ni}_{0.2}\text{O}_2$ using the ptychography technique.^[30–32] Despite the advantages offered by imaging with a high signal-to-noise ratio and low electron dose, this technique also poses strict requirements for sample thickness and requires a considerable amount of image post-processing. After the first observation of light elements using the ABF imaging technique in 2009,^[33] several studies have been conducted to image lithium in LCO^[17,34,35] and in other lithium-containing CAMs.^[36–42] A simulation study on atomic-resolution imaging conditions for lithium was carried out by Findlay et al., showing the possibility to image lithium in lithium-containing compounds in different zone axes.^[43] However, the effects of experimental factors like nontrivial sample preparation, ion- and electron-beam damage, and detector noise have not been taken into account in this study. More recent work by Findlay et al.^[44] showed that by subtracting the medium angle bright-field (MABF) intensity from the ABF intensity, the contrast of lighter atoms against the background is enhanced. This happens because light elements produce strong signals in the MABF regime due to electron channelling.^[45] This idea of combining intensities at different angular ranges was first put forward by Rose et al.^[46,47]

Electron energy loss spectroscopy (EELS) has also been employed to detect lithium by using the lithium K-edge.^[48] However, the lithium K-edge is in the low loss regime, making it highly delocalized, and acquiring atomically resolved spectra is only possible if the lithium columns are far apart from one another.^[43] Since transition metals are used in most battery compounds, the overlap of their $M_{2,3}$ edges with the lithium K-edge further complicates the analysis.^[49,50]

Moreover, the majority of studies on imaging lithium were carried out on individual single-crystalline nanoparticles,^[34,17] or on epitaxially grown single-crystalline thin films.^[35] Realistic CAMs, however, contain micrometer-sized secondary particles, composed of densely packed primary (nanocrystalline) particles (see Figure S1 in the Supporting Information).^[51] This makes sample preparation for electron microscopy challenging because of the heterogeneous morphology. The curtaining effect—a variation of sample thickness during ion-milling in different regions due to both voids present between the grains

and the arrangement of randomly oriented grains—is unavoidable.^[52] Furthermore, the polycrystalline nature of the secondary particles makes the following STEM analysis nontrivial. It is difficult to thin down the material to the necessary thickness and to analyse it in the preferred zone axis. For these reasons, an experimental study on realistic samples is missing and much needed to draw meaningful conclusions on phase-transformation mechanisms that may affect the battery performance.

In this work, we demonstrate a synergistic combination of different STEM techniques using a pixelated detector [4D STEM]. It allows atomically-resolved imaging of all elements, including lithium, in LNO (in a realistic sample, see Figure S2 in the Supporting Information). Utilizing the ability to see the same region using different STEM techniques simultaneously at atomic resolution, we gain meaningful information on the mechanism of phase transition. This is a paramount step toward controlling or even avoiding adverse phase transformations in Ni-rich CAMs.

2. Results and Discussion

2.1. Imaging of All Atoms for Different TEM Specimen Thicknesses

Figure 1 shows HAADF, $-ABF$, and $-eABF$ (enhanced ABF, see Experimental Section for a description of the technique) images of LNO viewed in the [100] zone axis at an approximate specimen thickness of 58 nm. The $-ABF$ and $-eABF$ images have been reconstructed from 4D STEM datasets of a pixelated detector, whereas the HAADF images were collected simultaneously using an annular detector. The applied angular ranges for the respective images are given in the Experimental Section. Note that the contrast in the ABF and eABF images has been reversed for better visibility to produce the so-called $-ABF$ and $-eABF$ images, respectively. The insets in the images show magnified regions of the experimental images (green bordered) and the corresponding simulations (red bordered). As expected, the HAADF image in **Figure 1a** only shows the heavy nickel atoms and, with very low contrast against the background, the oxygen atoms. The $-ABF$ image in **Figure 1b** reveals all elements in the lattice at this specimen thickness. Further significant enhancement of the contrast of light elements against the background is found in the $-eABF$ image in **Figure 1c**.

For realistic samples, it is not always possible to prepare a TEM specimen of desired thickness. Hence, it is important to prove that both ABF and eABF imaging can give good contrast for all atoms for various specimen thicknesses. As the simulations shown in **Figure 1** reproduce the experimental observations well, we conducted image simulations for different specimen thicknesses up to 95 nm and extracted the contrast data for the different detector ranges. **Figure 2a–c** shows the simulated contrast evolution (as a function of specimen thickness) of the nickel, oxygen, and lithium atomic positions for the [100] orientation for the HAADF, $-ABF$, and $-eABF$ regimes, respectively. From **Figure 2a**, it is clear that it is not possible to see lithium using HAADF imaging. Also, the contrast of oxygen as compared to nickel is not sufficient to resolve the former satisfactorily at any thickness. This is primarily due to the close proximity of nickel. This contrast difference is drastically reduced for

Thickness ≈ 58 nm

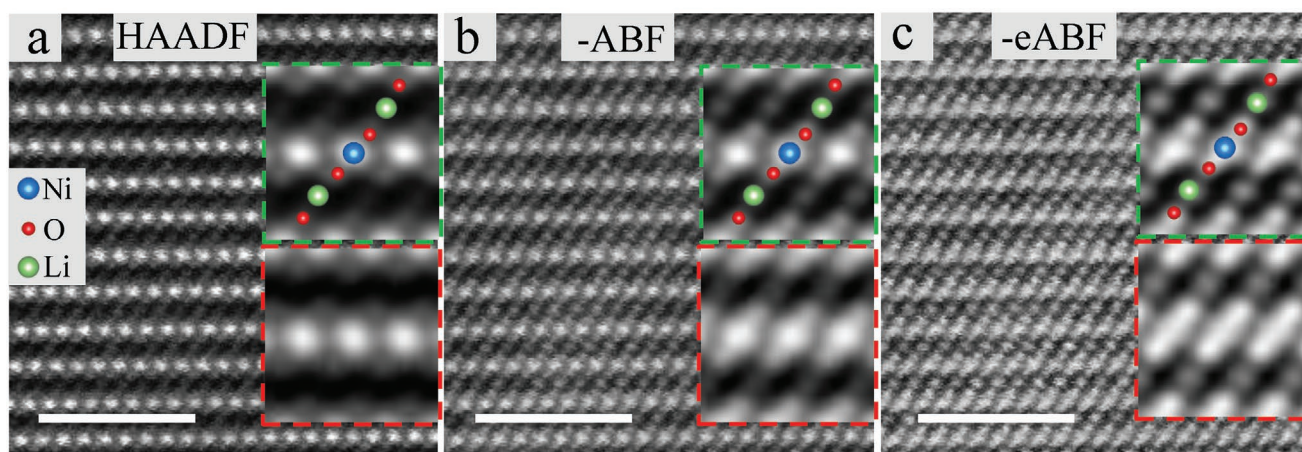


Figure 1. High-resolution a) HAADF, b) $-ABF$, and c) $-eABF$ images of LNO viewed in the $[100]$ orientation for a specimen thickness of around 58 nm. The green- and red-bordered insets are (magnified) averaged experimental and simulated images, respectively. The atom positions viewed in the $[100]$ orientation are shown in the green-bordered insets. Scale bars represent 2 nm.

the $-ABF$ technique, and now it is in fact feasible to visualize all atoms, as shown in Figure 2b. The improved visibility for all atoms stems from the reduced contrast of the nickel in this angular range. However, it is still not possible to clearly resolve

lithium atoms for larger specimen thicknesses. Figure 2c shows that this problem can be overcome by using the $-eABF$ technique. Here, the contrast from the lithium atoms is enhanced, particularly for smaller thicknesses. The contrast of nickel and

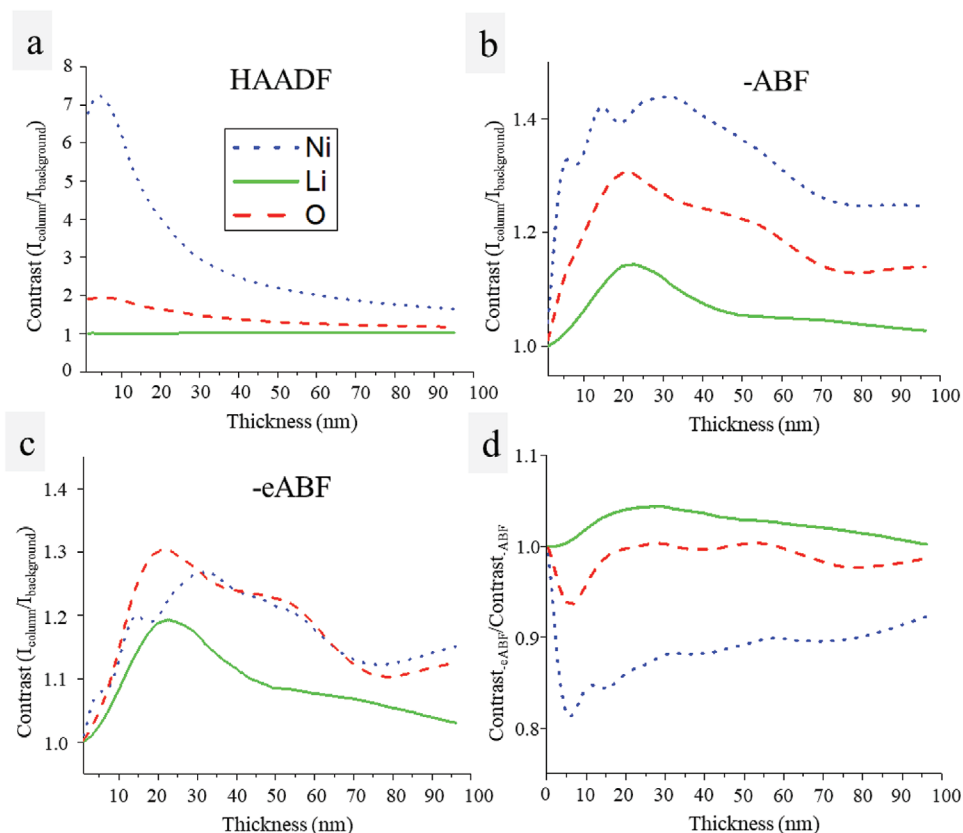


Figure 2. Contrast change of the nickel, lithium, and oxygen atomic positions as a function of TEM specimen thickness for the $[100]$ orientation of LNO: a) HAADF, b) $-ABF$, and c) $-eABF$. The contrast is evaluated by dividing the peak intensity at the atomic positions by the background intensity for each thickness. The background intensity is taken as the intensity at a position between two consecutive lithium positions. d) Comparison between $-eABF$ and $-ABF$. Values above, below, and equal to 1 show an increase, decrease, and no change in contrast, respectively, when comparing $-eABF$ to $-ABF$.

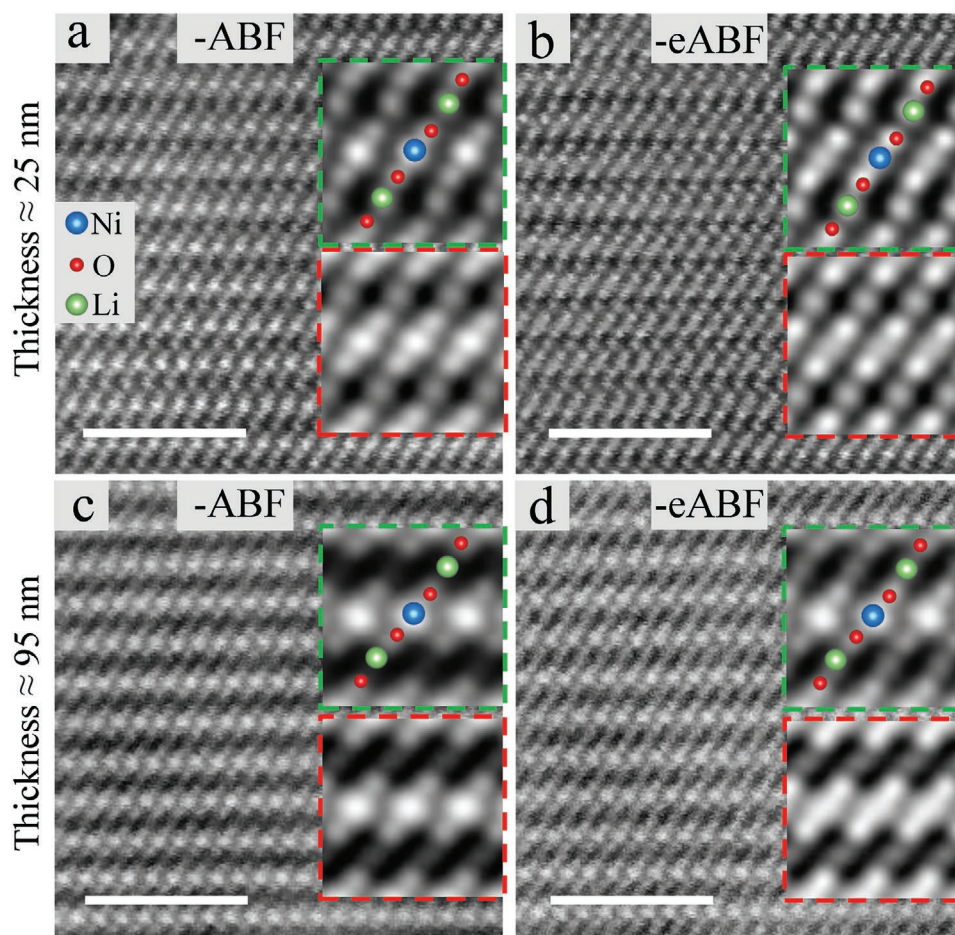


Figure 3. High-resolution $-ABF$ and $-eABF$ images of LNO viewed in the $[100]$ orientation for specimen thicknesses of a) and b) around 25 nm and c) and d) around 95 nm. The green- and red-bordered insets are (magnified) averaged experimental and simulated images, respectively. The atom positions in $[100]$ orientation are shown in the green-bordered insets. Scale bars represent 2 nm.

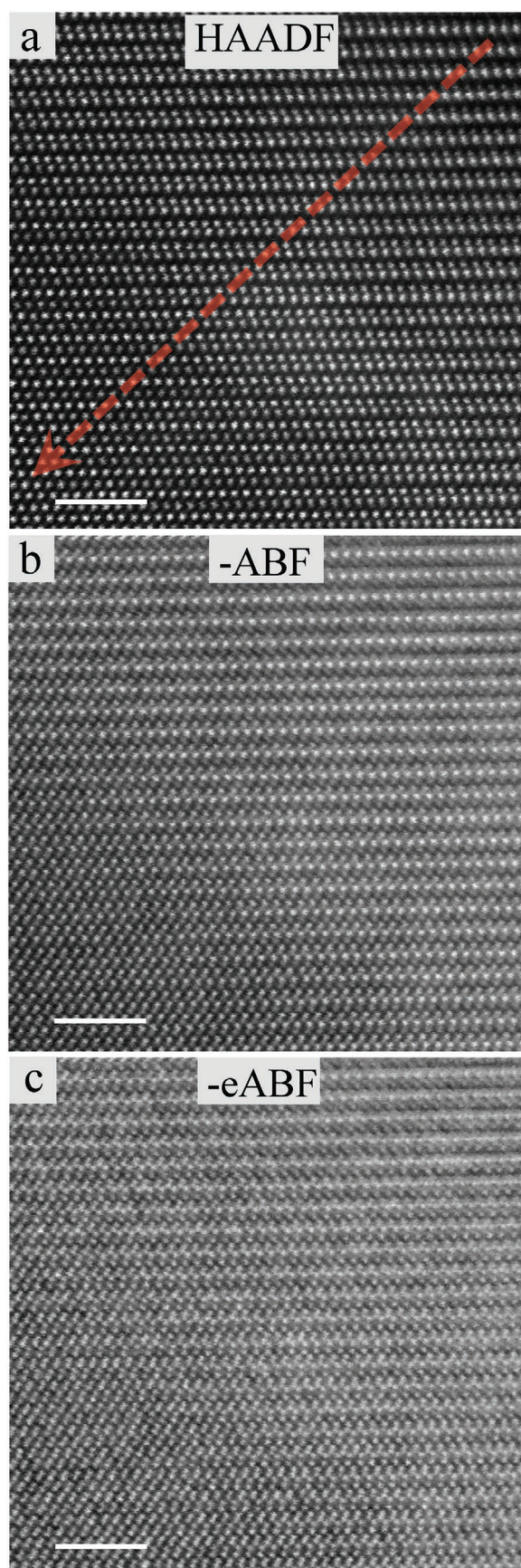
oxygen becomes similar, with the oxygen contrast surpassing that of nickel in the specimen thickness range between 10 and 30 nm. Figure 2d illustrates the difference in contrast between $-ABF$ and $-eABF$ as a function of specimen thickness. Here, the values above, below, and equal to 1 indicate an increase, decrease, and no change in contrast, respectively. The overall contrast enhancement effect in $-eABF$ comes from the reduction in contrast of nickel atoms and a slight increase in lithium contrast. Even for larger thicknesses, where lithium contrast is only slightly increased (compared to $-ABF$), the decrease in nickel contrast provides a significant advantage. Hence, this means that by comparing intensities extracted from different angular ranges from 4D STEM datasets at the respective atomic positions, all atoms can be imaged (for different sample thicknesses).

To experimentally confirm our simulations, $-ABF$ and $-eABF$ images were taken for specimen thicknesses of around 25, 58, and 95 nm. The data for the 58-nm-thick specimen are provided in Figure 1. **Figure 3a–d** shows $-ABF$ and $-eABF$ images of the 25 and 95-nm-thick sample, respectively. Experimental HAADF images are not shown in Figure 3, since there is little or no information about light elements (Figures 1a and 2a) that can be gained from such data. The $-ABF$ image in Figure 3a clearly shows all atoms in the structure, but the contrast from lithium

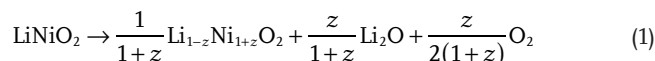
is higher in the $-eABF$ image in Figure 3b, thereby confirming the results of our simulations (Figure 2). The contrast trends for the 58-nm-thick specimen in Figure 1 are similar to those discussed for the 25-nm-thick sample. In Figure 3c (95-nm-thick sample), lithium atoms cannot be imaged clearly when using the $-ABF$ technique. However, they are revealed in the $-eABF$ image shown in Figure 3d. This opens up new possibilities of imaging challenging structural features involving light atoms, without depending excessively on sample thickness. In the following, we demonstrate the potential of the techniques by imaging the layered-to-rock salt phase transition in LNO.

2.2. Layered-to-Rock Salt Phase Transition

It is well known that the structure of LNO (and of most Ni-rich oxide CAMs) is unstable;^[8] several situations can induce a layered-to-rock salt transformation at the material's surface, extending several nanometer into the bulk. These include electrochemical cycling,^[53] temperature treatments at and above 700 °C (coinciding with the material's initial synthesis)^[28] or exposure to moisture in the atmosphere.^[54] Even pores within the primary particles were shown to possess boundaries of rock



salt-like structure.^[55] In general, the decomposition of LNO can be written as



However, the detailed reaction pathway to form the $\text{Li}_{1-z}\text{Ni}_{1+z}\text{O}_2$ phase, its actual composition, and whether intermediate reaction products exist are still unknown. Note that it can also be written as $\text{Li}_y\text{Ni}_{1-y}\text{O}$, indicating the decomposition product can be either layered or rock salt, depending on the extent of decomposition. Hence, we investigated phase-transformation regions in LNO using the above-described analysis to shed light on the atomistic processes. The sample used for the study is pristine, i.e., it did not undergo any electrochemical cycling. The presence of rock salt-like grain boundaries, as described in the following, originates directly from the synthesis process of the material (even though the material was prepared using an optimized procedure, see Experimental Section). A grain, which had partially undergone phase transformation, was selected for analysis. The specific region at low magnification (grain oriented in the [100] zone axis) is shown in Figure S3 in the Supporting Information. Figure S4 in the Supporting Information is a high-resolution HAADF image showing at large field-of-view (FOV) the layered region, the phase transition one, and the rock salt structure. Extreme care has been taken not to damage the LNO during sample preparation and STEM investigation. To prove that the phase-transformed region is not a result of ion- and electron-beam bombardment, STEM images of LNO showing distorted crystal regions resulting from severe electron/ion-beam bombardment are presented in Figure S5 in the Supporting Information for comparison. The damage to the material is distinctly different from the region seen in Figure S4 in the Supporting Information. Furthermore, the rock salt transformation emerging solely from electron-beam damage is markedly different, as shown by Lu et al.^[56]

Here, the phase transition region was probed using the HAADF, ABF, and eABF techniques. **Figure 4a–c** shows HAADF, –ABF, and –eABF images, respectively, from the layered-to-rock salt phase transition region. It is important to note that all images are obtained from a single acquisition utilizing the pixelated detector (for virtual –ABF and –eABF) and a conventional ADF detector (for HAADF) so the individual signals are spatially perfectly aligned to one another. As is evident, the phase transformation proceeds from the top right corner, being closest to the layered structure, toward the rock salt structure in a diagonal direction. The phase transformation front, denoted by an arrow in Figure 4a, appears to proceed perpendicular to the (104) facet of the particle. In order to confirm that the structure is not a simple projection of the LNO and NiO structures, a supercell was created by stacking the rock salt (NiO) structure on top of LNO. Figure S6 in the Supporting Information shows the supercell in different directions as well as the resulting simulated HAADF images for different specimen thicknesses.

Figure 4. High-resolution a) HAADF, b) –ABF, and c) –eABF images of the phase transition region viewed in the [100] orientation. The images were taken close to the grain boundary region denoted in Figure S3 in the Supporting Information. The red arrow indicates the direction of the layered-to-rock salt phase transformation. Scale bars represent 2 nm.

For a more detailed analysis, Figure 4a–c was divided into 16 different patches of 128 by 128 pixels each and averaged to obtain 16 images having 44 by 44 pixels (Figure S7, Supporting Information). This increased the signal-to-noise ratio considerably. In Figure 4a, a gradual increase in intensity in the vicinity of the positions corresponding to lithium in the layered structure is noticed when scanning across the phase transformation region (from top right to bottom left). Because nickel is the only heavy element in this material, thus showing bright contrast in the HAADF regime, this intensity increase is due

to gradual movement of nickel atoms towards the lithium position. We assume that the nickel ions proceed via the intermediate tetrahedral positions, considering that these are the only empty sites available in the structure. Hence, ion movement and hopping between neighboring octahedra must necessarily occur via an intermediate tetrahedral site. Hereafter, we refer to the nickel ions that are moving through tetrahedral positions to as Ni*. Figure 5a shows the model of the layered structure of LNO in [100] and the fully transformed rock salt in the corresponding [110] direction. The tetrahedral sites are shown by

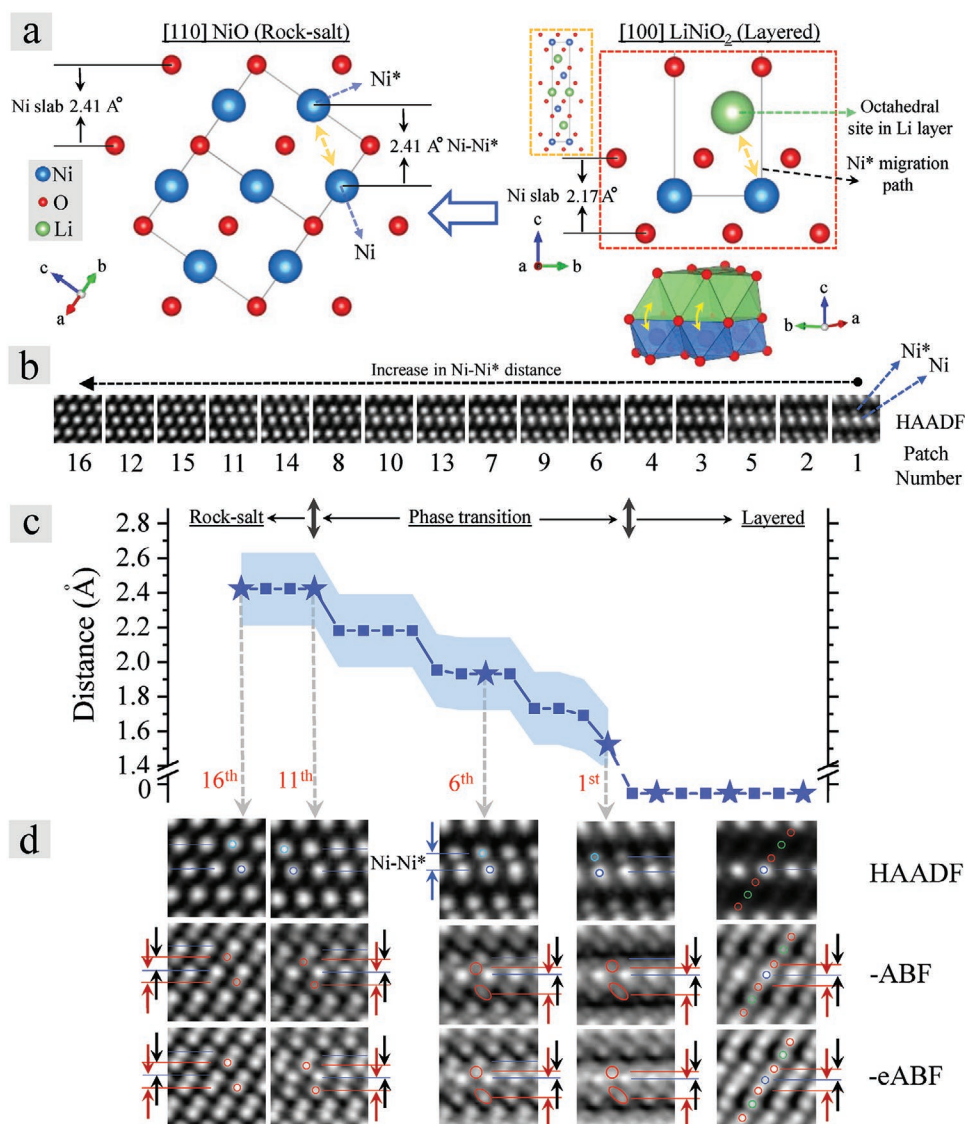


Figure 5. a) Crystal structures of NiO and LNO in [100] projection. Ni–Ni* distances projected along the *c*-axis and Ni slab thicknesses are shown. b) Arrangement of patches from the HAADF regime (Figure S7a, Supporting Information) in increasing order of Ni–Ni* distance from right to left. c) Blue curve showing the increase in Ni–Ni* distance from the layered structure (on the right) through the transition region (in the middle) toward the rock salt-like structure (on the left). The blue stars mark the distances in the patches shown below, which are in a diagonal direction in Figure S7a in the Supporting Information. The light blue band along the curve represents the error bar due to the pixel density limit (± 0.21 Å per pixel). d) Row arrangement of diagonal patches in HAADF, –ABF, and –eABF regimes, as shown in Figure S7 in the Supporting Information. The layered patches (on the right) are presented here for comparison only. The blue lines in the HAADF and red lines in the –ABF and –eABF patches are guides to the eye for Ni–Ni* distance and O–O distance, respectively. The blue, light blue, green, and red circles/ellipses denote the Ni, Ni*, Li, and O atomic positions, respectively. The red and black arrows in –ABF and –eABF patches indicate the distances between the O ions, which are above and below with respect to the Ni ions in the transition-metal layer.

yellow arrows in the respective structures and also in the polyhedral crystal model of the layered structure.

Using the patches from the HAADF image in Figure S7a in the Supporting Information, the distance between the Ni atoms and the Ni* atoms diffusing away from the regular position (projected along the *c*-axis) was measured. Note that the patches in Figure 5b are arranged in the order of increasing Ni–Ni* distance along the phase transition region. The blue curve in Figure 5c shows the increase in Ni–Ni* distance along the phase transition region, from layered towards the rock salt structure. Because the pixel density in these patches is limited to 0.21 Å per pixel and because of difficulties in accurately assigning the peak positions, a constant error of ± 0.21 Å has been assigned to each value measured along the curve. From the 11th patch onward, the Ni–Ni* distance is 2.4(2) Å, which is very close to the Ni–Ni* distance in the NiO rock salt structure in [110] direction (≈ 2.4 Å),^[28] and remains constant in the rock salt region (see also Figure S4 in the Supporting Information). This shows that the phase transformation is complete, as no more (measurable) changes in Ni–Ni* distances occur afterwards. Importantly, a transition region was detected (close to the 6th patch), where the Ni–Ni* distance is clearly lower than the 2.4 Å value mentioned above. In fact, Ni–Ni* distances of 1.8(2) Å were observed. Despite the notable error bar due to pixel resolution, this reduction is significant, and it is very close to the value expected if Ni* was placed in a tetrahedral site of the Li layer in the layered structure (1.81 Å). Hence, we conclude that, in the transition region, Ni* is located in the tetrahedral positions, which represent local but not absolute minima in the energy landscape of the layered structure.^[57–59] One may note that none of the computationally predicted surface structures in the Li–Ni–O phase diagram features tetrahedral Ni,^[12] which is a thermodynamically unlikely state because of the electronic structure of Ni that prefers a square planar geometry as 4-coordinated Ni²⁺ (d⁸ configuration).^[59,60] However, our observations suggest that, in the transition region, tetrahedral Ni may be locally and kinetically stabilized through the constraints placed by the lithiated layered structure on the one side and (nearly) delithiated rock salt phase on the other.

We further observed that, while nickel has to diffuse through the tetrahedral positions, this only takes place toward one side of the layered structure, which is upwards in this case (see 6th patch). We argue that this asymmetry is governed by the nearest (003) facet (marked by a red arrow in Figure S3 in the Supporting Information). This movement is in accordance with inward diffusion of Ni ions (densification), which usually takes place during phase transformation in combination with oxygen loss, as often suggested in the literature.^[61,62] In particular, oxygen loss (Equation (1)) results in oxygen vacancies, which have been shown to considerably reduce the energy barrier for Ni diffusion through tetrahedral positions.^[13,63] The asymmetry of Ni movement can be one of the reasons for discrepancy between our observations and computational methods, which typically deal with bulk properties.^[12,64]

The movement of Ni* in the HAADF images is not the sole asymmetry that is observable; we can also exploit –ABF and –eABF patches, focusing on oxygen ions in the phase transition region on either side of the primary Ni position in the transition-metal layer. The red lines in the –ABF and –eABF

patches mark the Ni slab thickness (Figure 5d). The black and red arrows indicate the distances of oxygen ions in the Ni slab with respect to the primary Ni position in the transition-metal layer (Ni–O distance projected along *c*), in the upper and the bottom layers, respectively. These distances are different from each other in the 1st and 6th patches, indicating a shift of the average O positions in the opposite direction with respect to the location of tetrahedral Ni*. As soon as tetrahedral Ni* peaks appear in the HAADF, the oxygen ions (in –ABF and –eABF) in the upper layer seem to be shifted to a lower position along the *c*-axis, somewhat closer to the primary Ni position. The oxygen ions in the bottom layer, on the other hand, are significantly shifted further away from the Ni positions, suggesting a local deformation of the Ni octahedral environment. Interestingly, the asymmetric process is in good agreement with what is expected from computations. For example, Kong et al.^[13] argue that the movement of Ni ions through the tetrahedral site, in the phase transformation region, is opposite to the oxygen layers in which oxygen vacancies are formed. Finally, we shall mention that we do not observe any indication suggesting the presence of a spinel structure in our images. Typically, in the Li–Ni–O chemical space, the only spinel structure would be expected to have a composition close to Li_{0.5}NiO₂, and Li would be located in tetrahedral sites, but not Ni. Contrarily, we observe tetrahedral Ni, stabilized asymmetrically with respect to the particles (003) facet. Although the contrast and resolution of our images is not sufficient to exclude the presence of also some Li being in tetrahedral sites, the observations described herein strongly point towards a reaction mechanism where local constraints, rather than bulk thermodynamics, play a dominant role. In NCM materials, on the other hand, the presence of a significant amount of Mn and Co, both forming very stable spinel structures (LiMn₂O₄ and Co₃O₄, respectively), may result in the observation of intermediate spinel regions between the layered and rock salt ones.^[14]

Taken together, the imaging data and subsequent analysis presented in this work are important steps toward better understanding the layered-to-rock salt phase transformation in LNO, which cannot be uncovered by X-ray diffraction and conventional high-resolution electron microscopy techniques like HAADF.

3. Conclusions

In this study, we have successfully explored the use of a pixelated detector to image light atoms in the lithium-ion battery cathode active material LNO. A sample was studied for several TEM specimen thicknesses using the HAADF, ABF, and eABF imaging techniques. ABF revealed good sensitivity to lithium and oxygen atoms for small specimen thickness. The contrast of light elements was demonstrated experimentally for the first time to be significantly improved by eABF imaging, especially for larger specimen thicknesses. We also showed that from HAADF, –ABF, and –eABF images of the same area, specific insights into phase transformation regions can be gained. The analysis of the layered-to-rock salt phase transition region suggested that there is no sharp interface between the structures. Instead, the transformation appears to take place gradually. In the transition region, no indication for a local structure with spinel symmetry

is found. On the other hand, we observed the presence of nickel ions on tetrahedral sites diffusing inwards from the particle's surface. Oxygen appears to be asymmetrically displaced toward the surface, thereby locally distorting the nickel octahedral environment. We believe that the transition steps shown here can be of help for engineering new materials with improved structural stability, possibly via doping strategies with elements selected for their likelihood to be located in tetrahedral sites. Moreover, the results may act as a guide to direct further computational studies about the near-surface stability in LNO-based materials.

4. Experimental Section

The LiNiO_2 cathode material was prepared by solid-state synthesis using commercial NiO as precursor (Alfa Aesar, 99.998%) and $\text{LiOH}\cdot\text{H}_2\text{O}$ (BASF SE) as lithium source. The powders were mixed without grinding and placed in alumina crucibles, followed by annealing in a tube furnace at 700 °C for 6 h under O_2 flow. The resultant sample was then quickly transferred into an Ar-filled glovebox and sieved using a 45 μm mesh.

TEM sample preparation was carried out using a JEOL JIB 4601F multibeam system using the focused ion beam (FIB) preparation technique.^[65] Figure S1 in the Supporting Information shows the secondary particle selected for TEM sample preparation. It was thinned down to about 250 nm with a 30 kV Ga-ion beam and then to 95 nm with a 5 kV beam (Figure S2, Supporting Information). This was followed by further low-energy milling (Fischione Model 1040 NanoMill) down to thicknesses of about 58 and 25 nm using 900 and 500 eV Ar-ion beams, respectively.

4D STEM datasets were collected using a double aberration-corrected JEOL JEM-2200FS microscope combined with a pnCCD^[66,67] pixelated detector after each thinning step. An operating voltage of 200 kV was used with a 15.07 mrad convergence semiangle of the probe. The pnCCD was operated in fourfold binning mode, with a dwell time of 250 μs per pixel. Virtual ABF images were obtained by using inner and outer virtual aperture angles of 8 and 16 mrad, respectively. eABF images were then obtained by subtracting MaBF,^[44] obtained by using inner and outer angles of 0 and 8 mrad, from the ABF images. Creating virtual eABF images from a pixelated detector excludes the need for careful relative calibration and normalization of two separate detectors. It is important to note that—although a pixelated detector has been used to acquire 4D STEM datasets—it was believed that comparable results can be obtained using carefully arranged conventional ADF and BF detectors to implement eABF imaging. However, of course, the access to the full diffraction pattern and several postimaging data processing capabilities would be lost. Moreover, the high signal-to-noise ratio of the pixelated detector is not accessible with conventional annular detectors. In addition, corresponding HAADF images were acquired using a conventional ADF detector with inner and outer angles of 70 and 180 mrad, respectively. All images shown in the manuscript are in the [100] direction, as the O3 ordering and the layered structure can only be seen in [100]-type zone axis in LiNiO_2 with good resolution to separate all atoms. A constant dose of $16.72 \times 10^6 \text{ e}^- \text{ nm}^{-2}$ was measured over a FOV of $11.06 \text{ nm} \times 11.06 \text{ nm}$ for all high-resolution images, except Figures S4 and S5 in the Supporting Information. To minimize the electron dose, the lowest possible experimentally available convergence semiangle of 15.07 mrad was used. The atomically resolved images obtained in the [100] orientation are from the grain shown in Figure S3 (Supporting Information), with approximate thicknesses of 95, 58, and 25 nm, respectively.

STEM simulations were carried out using the multislice algorithm, implemented in the STEMSalabim code.^[68,69] In accordance with the experiment, an operating voltage of 200 kV was used, with a convergence semi-angle of 15.07 mrad and residual geometric aberrations of $D_f = 0 \text{ nm}$, $C_s = 2 \mu\text{m}$, and $S_5 = 5 \text{ mm}$. For each simulation, a defocus series consisting of 7 weighted defoci centred around the optimum defocus was calculated to model the effects of chromatic aberration.^[70] For each defocus, ten individual frozen phonon configurations were averaged. In

the simulations in Figure S6 (Supporting Information), defocus series and frozen phonon configurations have not been taken into account.

All high-resolution ABF and eABF images are presented with an inverted contrast for better visualization of the atoms. In the text, they are referred to as $-\text{ABF}$ and $-\text{eABF}$ images. It is important to note that no filtering has been applied to any image shown in the paper. The insets marked with green-bordered squares in Figures 1 and 3 and the patches in Figure 5 and Figure S7 (Supporting Information) are averaged images formed from many subimages obtained by dividing up the full images. This method has been described by Beyer et al.^[71]

Supporting Information

Supporting Information is available from the Wiley Online Library or from the author.

Acknowledgements

S.A., M.B., and A.P. contributed equally to this work. The authors acknowledge funding by BMBF (Bundesministerium für Bildung und Forschung) in the framework of the FESTBATT competence cluster (project 03XP0176C) as well as in the framework of the MehrSi project (03SF0525C). M.M., A.B., and K.V. acknowledge funding from the German Research Foundation in the framework of the SFB 1083 (Structure and Dynamics of Internal Interfaces). M.B., T.B., P.H., and J.J. acknowledge financial support of BASF SE. The work was partially carried out with the support of the Karlsruhe Nano Micro Facility (KNMF, www.knmf.kit.edu), a Helmholtz research infrastructure at Karlsruhe Institute of Technology (KIT, www.kit.edu).

Conflict of Interest

The authors declare no conflict of interest.

Keywords

4D scanning TEM, Li-ion batteries, LNO, phase transformations

Received: March 20, 2020

Revised: April 21, 2020

Published online:

- [1] N. Nitta, F. Wu, J. T. Lee, G. Yushin, *Mater. Today* **2015**, *18*, 252.
- [2] Y. Nishi, in *Lithium-Ion Battery* (Ed.: G. Pistoia), Elsevier, Amsterdam **2014**, pp. 21–39.
- [3] F. Schipper, E. M. Erickson, C. Erk, J.-Y. Shin, F. F. Chesneau, D. Aurbach, *J. Electrochem. Soc.* **2017**, *164*, A6220.
- [4] J. Xu, F. Lin, M. M. Doeff, W. Tong, *J. Mater. Chem. A* **2017**, *5*, 874.
- [5] L. de Biasi, B. Schwarz, T. Brezesinski, P. Hartmann, J. Janek, H. Ehrenberg, *Adv. Mater.* **2019**, *31*, 1900985.
- [6] H. Li, N. Zhang, J. Li, J. R. Dahn, *J. Electrochem. Soc.* **2018**, *165*, A2985.
- [7] U.-H. Kim, D.-W. Jun, K.-J. Park, Q. Zhang, P. Kaghazchi, D. Aurbach, D. T. Major, G. Goobes, M. Dixit, N. Leifer, C. M. Wang, P. Yan, D. Ahn, K.-H. Kim, C. S. Yoon, Y.-K. Sun, *Energy Environ. Sci.* **2018**, *11*, 1271.
- [8] M. Bianchini, M. Roca-Ayats, P. Hartmann, T. Brezesinski, J. Janek, *Angew. Chem., Int. Ed.* **2019**, *58*, 10434.
- [9] L. de Biasi, A. Schiele, M. Roca-Ayats, G. Garcia, T. Brezesinski, P. Hartmann, J. Janek, *ChemSusChem* **2019**, *12*, 2240.

- [10] A. Manthiram, in *Lithium Batter. Sci. Technol.* (Eds.: G.-A. Nazri, G. Pistoia), Springer, US **2003**, pp. 3–41.
- [11] J. Xu, E. Hu, D. Nordlund, A. Mehta, S. N. Ehrlich, X.-Q. Yang, W. Tong, *ACS Appl. Mater. Interfaces* **2016**, *8*, 31677.
- [12] H. Das, A. Urban, W. Huang, G. Ceder, *Chem. Mater.* **2017**, *29*, 7840.
- [13] F. Kong, C. Liang, L. Wang, Y. Zheng, S. Peranathan, R. C. Longo, J. P. Ferraris, M. Kim, K. Cho, *Adv. Energy Mater.* **2019**, *9*, 1802586.
- [14] N. Y. Kim, T. Yim, J. H. Song, J.-S. Yu, Z. Lee, *J. Power Sources* **2016**, *307*, 641.
- [15] Y. Gong, Y. Chen, Q. Zhang, F. Meng, J.-A. Shi, X. Liu, X. Liu, J. Zhang, H. Wang, J. Wang, Q. Yu, Z. Zhang, Q. Xu, R. Xiao, Y.-S. Hu, L. Gu, H. Li, X. Huang, L. Chen, *Nat. Commun.* **2018**, *9*, 3341.
- [16] A. K. Shukla, Q. M. Ramasse, C. Ophus, D. M. Kepaptsoglou, F. S. Hage, C. Gammer, C. Bowling, P. A. H. Gallegos, S. Venkatachalam, *Energy Environ. Sci.* **2018**, *11*, 830.
- [17] Y. Gong, J. Zhang, L. Jiang, J.-A. Shi, Q. Zhang, Z. Yang, D. Zou, J. Wang, X. Yu, R. Xiao, Y.-S. Hu, L. Gu, H. Li, L. Chen, *J. Am. Chem. Soc.* **2017**, *139*, 4274.
- [18] P.-V. Ong, Z. Yang, P. V. Sushko, Y. Du, *J. Phys. Chem. Lett.* **2018**, *9*, 5515.
- [19] P. Yan, J. Zheng, Z.-K. Tang, A. Devaraj, G. Chen, K. Amine, J.-G. Zhang, L.-M. Liu, C. Wang, *Nat. Nanotechnol.* **2019**, *14*, 602.
- [20] S. Lee, W. Jin, S. H. Kim, S. H. Joo, G. Nam, P. Oh, Y.-K. Kim, S. K. Kwak, J. Cho, *Angew. Chem., Int. Ed.* **2019**, *58*, 10478.
- [21] B. Xiao, K. Wang, G.-L. Xu, J. Song, Z. Chen, K. Amine, D. Reed, M. Sui, V. Sprenkle, Y. Ren, P. Yan, X. Li, *Adv. Mater.* **2019**, *31*, 1805889.
- [22] P. D. Nellist, S. J. Pennycook, in *Adv. Imaging Electron Phys.* (Ed.: P. W. Hawkes), Elsevier, Amsterdam **2000**, pp. 147–203.
- [23] E. Yücelen, I. Lazić, E. G. T. Bosch, *Sci. Rep.* **2018**, *8*, 2676.
- [24] P. D. Nellist, in *Scanning Transm. Electron Microsc. Imaging Anal.* (Eds.: S. J. Pennycook, P. D. Nellist), Springer-Verlag, New York **2011**, pp. 91–115.
- [25] J. G. Lozano, G. T. Martinez, L. Jin, P. D. Nellist, P. G. Bruce, *Nano Lett.* **2018**, *18*, 6850.
- [26] S. D. Findlay, N. Shibata, H. Sawada, E. Okunishi, Y. Kondo, Y. Ikuhara, *Ultramicroscopy* **2010**, *110*, 903.
- [27] Y. Oshima, S. Lee, K. Takayanagi, *Microscopy* **2017**, *66*, 15.
- [28] M. Bianchini, F. Fauth, P. Hartmann, T. Brezesinski, J. Janek, *J. Mater. Chem. A* **2019**, *8*, 1808.
- [29] Y. Shao-Horn, L. Croguennec, C. Delmas, E. C. Nelson, M. A. O’Keefe, *Nat. Mater.* **2003**, *2*, 464.
- [30] J. M. Rodenburg, R. H. T. Bates, *Philos. Trans. R. Soc., A* **1992**, *339*, 521.
- [31] H. Yang, I. MacLaren, L. Jones, G. T. Martinez, M. Simson, M. Huth, H. Ryll, H. Soltau, R. Sagawa, Y. Kondo, C. Ophus, P. Ercius, L. Jin, A. Kovács, P. D. Nellist, *Ultramicroscopy* **2017**, *180*, 173.
- [32] H. Yang, R. N. Rutte, L. Jones, M. Simson, R. Sagawa, H. Ryll, M. Huth, T. J. Pennycook, M. L. H. Green, H. Soltau, Y. Kondo, B. G. Davis, P. D. Nellist, *Nat. Commun.* **2016**, *7*, 12532.
- [33] E. Okunishi, I. Ishikawa, H. Sawada, F. Hosokawa, M. Hori, Y. Kondo, *Microsc. Microanal.* **2009**, *15*, 164.
- [34] X. Lu, Y. Sun, Z. Jian, X. He, L. Gu, Y.-S. Hu, H. Li, Z. Wang, W. Chen, X. Duan, L. Chen, J. Maier, S. Tsukimoto, Y. Ikuhara, *Nano Lett.* **2012**, *12*, 6192.
- [35] R. Huang, T. Hitosugi, S. D. Findlay, C. A. J. Fisher, Y. H. Ikuhara, H. Moriwake, H. Oki, Y. Ikuhara, *Appl. Phys. Lett.* **2011**, *98*, 051913.
- [36] L. Gu, C. Zhu, H. Li, Y. Yu, C. Li, S. Tsukimoto, J. Maier, Y. Ikuhara, *J. Am. Chem. Soc.* **2011**, *133*, 4661.
- [37] C. Zhu, L. Gu, L. Suo, J. Popovic, H. Li, Y. Ikuhara, J. Maier, *Adv. Funct. Mater.* **2014**, *24*, 312.
- [38] R. Wang, X. He, L. He, F. Wang, R. Xiao, L. Gu, H. Li, L. Chen, *Adv. Energy Mater.* **2013**, *3*, 1358.
- [39] X. Lu, L. Zhao, X. He, R. Xiao, L. Gu, Y.-S. Hu, H. Li, Z. Wang, X. Duan, L. Chen, J. Maier, Y. Ikuhara, *Adv. Mater.* **2012**, *24*, 3233.
- [40] R. Huang, Y. H. Ikuhara, T. Mizoguchi, S. D. Findlay, A. Kuwabara, C. A. J. Fisher, H. Moriwake, H. Oki, T. Hirayama, Y. Ikuhara, *Angew. Chem., Int. Ed.* **2011**, *50*, 3053.
- [41] L. Suo, W. Han, X. Lu, L. Gu, Y.-S. Hu, H. Li, D. Chen, L. Chen, S. Tsukimoto, Y. Ikuhara, *Phys. Chem. Chem. Phys.* **2012**, *14*, 5363.
- [42] X. Gao, Y. H. Ikuhara, C. A. J. Fisher, H. Moriwake, A. Kuwabara, H. Oki, K. Kohama, R. Yoshida, R. Huang, Y. Ikuhara, *Adv. Mater. Interfaces* **2014**, *1*, 1400143.
- [43] S. D. Findlay, N. R. Lugg, N. Shibata, L. J. Allen, Y. Ikuhara, *Ultramicroscopy* **2011**, *111*, 1144.
- [44] S. D. Findlay, Y. Kohno, L. A. Cardamone, Y. Ikuhara, N. Shibata, *Ultramicroscopy* **2014**, *136*, 31.
- [45] M. Ohtsuka, T. Yamazaki, Y. Kotaka, I. Hashimoto, K. Watanabe, *Ultramicroscopy* **2012**, *120*, 48.
- [46] H. Rose, *Optik* **1974**, *39*, 416.
- [47] M. Hammel, H. Rose, *Ultramicroscopy* **1995**, *58*, 403.
- [48] J. Kikkawa, T. Mizoguchi, M. Arai, T. Nagai, K. Kimoto, *Phys. Rev. B* **2018**, *98*, 075103.
- [49] S. Muto, K. Tatsumi, T. Sasaki, H. Kondo, T. Ohsuna, K. Horibuchi, Y. Takeuchi, *Electrochem. Solid-State Lett.* **2010**, *13*, A115.
- [50] V. Mauchamp, F. Boucher, G. Ouvrard, P. Moreau, *Phys. Rev. B* **2006**, *74*, 115106.
- [51] P. Yan, J. Zheng, M. Gu, J. Xiao, J.-G. Zhang, C.-M. Wang, *Nat. Commun.* **2017**, *8*, 14101.
- [52] J.-Y. Kim, Y. W. Jeong, H. Y. Cho, H. J. Chang, *Appl. Microsc.* **2017**, *47*, 77.
- [53] J. Xu, F. Lin, D. Nordlund, E. J. Crumlin, F. Wang, J. Bai, M. M. Doeff, W. Tong, *Chem. Commun.* **2016**, *52*, 4239.
- [54] D. Pritzl, T. Teufl, A. T. S. Freiberg, B. Strehle, J. Sicklinger, H. Sommer, P. Hartmann, H. A. Gasteiger, *J. Electrochem. Soc.* **2019**, *166*, A4056.
- [55] S. Ahmed, A. Pokle, S. Schweidler, A. Beyer, M. Bianchini, F. Walther, A. Mazilkin, P. Hartmann, T. Brezesinski, J. Janek, K. Volz, *ACS Nano* **2019**, *13*, 10694.
- [56] P. Lu, P. Yan, E. Romero, E. D. Spoecker, J.-G. Zhang, C.-M. Wang, *Chem. Mater.* **2015**, *27*, 1375.
- [57] S.-M. Bak, E. Hu, Y. Zhou, X. Yu, S. D. Senanayake, S.-J. Cho, K.-B. Kim, K. Y. Chung, X.-Q. Yang, K.-W. Nam, *ACS Appl. Mater. Interfaces* **2014**, *6*, 22594.
- [58] S.-M. Bak, K.-W. Nam, W. Chang, X. Yu, E. Hu, S. Hwang, E. A. Stach, K.-B. Kim, K. Y. Chung, X.-Q. Yang, *Chem. Mater.* **2013**, *25*, 337.
- [59] J. Reed, G. Ceder, *Chem. Rev.* **2004**, *104*, 4513.
- [60] F. A. Cotton, G. Wilkinson, C. A. Murillo, M. Bochmann, *Advanced Inorganic Chemistry*, Wiley, USA **1999**.
- [61] A. Boulineau, L. Simonin, J.-F. Colin, C. Bourbon, S. Patoux, *Nano Lett.* **2013**, *13*, 3857.
- [62] A. Boulineau, L. Simonin, J.-F. Colin, E. Canévet, L. Daniel, S. Patoux, *Chem. Mater.* **2012**, *24*, 3558.
- [63] E. Lee, K. A. Persson, *Adv. Energy Mater.* **2014**, *4*, 1400498.
- [64] P. Xiao, T. Shi, W. Huang, G. Ceder, *ACS Energy Lett.* **2019**, *4*, 811.
- [65] M. Schaffer, B. Schaffer, Q. Ramasse, *Ultramicroscopy* **2012**, *114*, 62.
- [66] H. Ryll, M. Simson, R. Hartmann, P. Holl, M. Huth, S. Ihle, Y. Kondo, P. Kotula, A. Liebel, K. Müller-Caspary, A. Rosenauer, R. Sagawa, J. Schmidt, H. Soltau, L. Strüder, *J. Instrum.* **2016**, *11*, P04006.
- [67] H. Ryll, K. Müller, S. Ihle, H. Soltau, I. Ordavo, A. Liebel, R. Hartmann, A. Rosenauer, L. Strüder, *Microsc. Microanal.* **2013**, *19*, 1160.
- [68] J. O. Oelerich, L. Duschek, J. Belz, A. Beyer, S. D. Baranovskii, K. Volz, *Ultramicroscopy* **2017**, *177*, 91.
- [69] P. Küelhan, A. Beyer, C. Fuchs, M. J. Weseloh, S. W. Koch, W. Stolz, K. Volz, *J. Microsc.* **2017**, *268*, 259.
- [70] C. Dwyer, C. Maunders, C. L. Zheng, M. Weyland, P. C. Tiemeijer, J. Etheridge, *Appl. Phys. Lett.* **2012**, *100*, 191915.
- [71] A. Beyer, R. Straubinger, J. Belz, K. Volz, *J. Microsc.* **2016**, *262*, 171.